FLOW DEPENDENT RELATIVE PERMEABILITY SCALING FOR STEADY-STATE TWO-PHASE FLOW IN POROUS MEDIA: LABORATORY VALIDATION ON A MICROFLUIDIC NETWORK

Marios S. Valavanides[1], Nikolaos Karadimitriou[2] and Holger Steeb[2],

[1] Dept. of Civil Engineering, University of West Attica, Greece

[2] Institute of Applied Mechanics, University of Stuttgart, Germany

This paper was prepared for presentation at the SPWLA 63rd Annual Logging Symposium held in Stavanger, Norway, June 10-15, 2022.

ABSTRACT

Conventionally, the relative permeabilities of two immiscible fluid phases flowing in porous media are considered and expressed as functions of saturation. Yet, this has been put into challenge by theoretical, numerical and laboratory studies of flow in artificial pore network models and real porous media. These works have revealed a significant dependency of the relative permeabilities on the flow rates, especially when the flow regime is capillary to capillary-viscous dominated, and part of the disconnected non-wetting phase (NWP) remains mobile. These studies suggest that relative permeability models should include the functional dependence on flow intensities. However, revealing the explicit form of such dependence remains a persistent problem. Just recently, a general form of dependence was inferred, based on extensive simulations with the *DeProF* model for steady-state two-phase flows in pore networks. The simulations revealed a systematic dependence of the relative permeabilities on the local flow rate intensities. This dependence can be described analytically by a universal scaling functional form of the actual independent variables of the process, namely, the capillary number, Ca, and the flow rate ratio, r. The proposed scaling comprises a kernel function accounting for the transition between capillarity- and viscosity-dominated flow phenomena. In a follow-up systematic laboratory study SCAL measurements provided a preliminary proof-of-concept on the applicability of the model and validated its specificity.

In the laboratory study presented here, we examine the applicability of the basic flow-rate dependent relative permeability scaling model in immiscible two-phase flows in an artificial two-dimensional microfluidic network, across different flow regimes.

In particular, we assess the applicability of the flow-dependent relative permeability scaling model in a microfluidic pore-network and we correlate the form of the associated kernel function with the interstitial structure of the flow across different flow regimes. The scope is to assess the applicability and/or universality of the aforementioned scaling function and to examine the forensic character of the kernel function, i.e. the potential for revealing the interstitial flow structure.

The proposed scaling opens new possibilities in improving SCAL protocols and other important applications, e.g. characterization of systems and flow conditions, rock typing, assessment of end-effects during R/SCAL, as well as the development of more efficient field-scale simulators.

INTRODUCTION

The conventional use of saturation as the independent variable in two-phase flow in porous media (PM) is based on the oversimplifying assumption that disconnected fluidic elements of the non-wetting phase (NWP) i.e. ganglia and droplets, do not move with the average flow but remain stranded in the porous medium matrix. This situation arises when flow conditions of 'relatively small values' of the capillary number are maintained. In those cases, the disconnected NWP fluidic elements block part of the cross-section available to the flow by a fraction analogous to the average saturation and effect a relative reduction of the permeability of both the NWP and the wetting phase (WP). Nevertheless, there is ample experimental evidence that disconnected flow is a substantial and sometimes prevailing flow pattern (Tsakiroglou *et al.*, 2007; Tallakstad *et al.*, 2009; Guillen *et al.*, 2012; Georgiadis *et al.*, 2013; Aursjo *et al.*, 2014; Datta *et al.*, 2014; Oughanem *et al.*, 2015; Armstrong *et al.*, 2016).

Treating relative permeabilities as functions of the saturation has been shown to be inefficient in providing a correct and specific-enough description of the process across the domain of all possible flow conditions, as extensively discussed by Valavanides (2018b). A particular value in saturation does not necessarily imply that a unique disconnected structure of the NWP will settle-in. Disconnected structures of the NWP can be coarsely described by a spectrum of population density distributions, extending from distributions of 'many-and-small' fluidic elements, e.g. droplets and small ganglia, to 'fewer-and-larger' fluidic elements e.g. small and large ganglia. For any one of those cases, the corresponding superficial velocity of the disconnected NWP would not necessarily attain the same value. The latter would be the result of the antagonism between the two factors inhibiting the transport of each phase, i.e. viscosity and capillarity, over the mass and momentum balances.

Flow conditions have an adverse effect on the momentum balance and, in particular, on the relevant magnitude of the Stokes flow resistances, due to the bulk viscosity of the NWP and WP, and to Young-Laplace resistances, due to the contact forces between the N/W menisci and the pore walls. The former depend on local (micro /pore scale) velocity gradients, in contrast to the latter that are relatively independent of the displacement rates of the menisci. From an energy point of view, the power dissipation, due to bulk viscosity, scales with the square of the local velocity gradients, whereas the capillarity-induced dissipation scales with the rates of displacement of the menisci. For relatively low values of the superficial velocity, viscosity effects are insignificant compared to capillarity effects; as flow intensity is progressively increased, viscosity takes over from capillarity and the flow progressively mutates from capillarity-dominated to transient capillary-viscosity- to viscosity-dominated characteristics (Valavanides, 2018b).

As a consequence, for any two different cluster configurations, i.e. any two different population density size distributions of disconnected phase, the effective permeabilities of the WP and the NWP would differ. Yet, those different cluster configurations and different values of the relative permeabilities could -in general- correspond to the same saturation value. In such situations, a universal, saturation-dependent description of the flow would be weak.

In addition, during core analysis, saturation is measured indirectly and cannot be externally imposed directly; it is only through control of a combination of pressure difference and/or flow rate of the NWP or the WP that the system will attain an average saturation. If one wants to consistently and systematically describe the process in the entire flow regime, extending across the broadest possible domain of the capillary number and the viscosity ratio, one has to consider those variables that describe the externally imposed conditions and contain macroscopic kinematic information; the superficial velocity of each phase or, equivalently, the capillary number and the flow rate ratio are such variables. Moreover, saturation cannot adequately, or uniquely, describe the flow conditions. This is because saturation alone brings no definite input to the momentum balance, therefore it is questionable if it can provide any information on the kinetics of the macroscopic flow.

Observations of single-phase flows within pore networks confirm that the macroscopic pressure gradient scales linearly with the superficial fluid velocity, as it is described by Darcy's law. This seems to be a quite trustworthy modeling consideration in the case of two-phase flow as well, but only when very high superficial velocities are considered, and capillary forces are negligible. However, at moderate/low velocities, when capillary forces are comparable to viscous forces, the macroscopic pressure gradient does not scale linearly with the flow rate. Experimental studies on steady-state two-phase flows in glass beads (Tallakstad *et al.*, 2009; Aursjo *et al.*, 2014; Datta *et al.*, 2014), in glass bead columns (Sinha *et al*, 2017), as well as in sand-pack columns (Tsakiroglou *et al.*, 2015), revealed that the non-linear relation between the pressure gradient and the flow rate can be described by generic power laws with different exponent values. The discrepancy between the values of the scaling exponents is attributed to differences associated with the dimensionality of the pertinent variables, measurements pertaining to different flow conditions, dimensionality of the NWP/WP/PM system etc. Therefore, it is worth the effort to examine if these 'different' observations can be integrated in a universal power law relating appropriate, dimensionless variables of the process.

To this end, a first attempt in deriving a universal scaling functional form describing the flow dependency of relative permeability was proposed (Valavanides, 2018c). It is based on the results from systematic, extensive simulations spanning over 5 orders of magnitude for both the capillary number and flow rate ratio, implementing the *DeProF* model algorithm, build around a hybrid, true-to-mechanism, stochastic scale-up model for steady-state two-phase flows in pore networks (Valavanides, 2018a).

In the present work we examine the applicability of the flow-rate dependent relative permeability scaling model, proposed by Valavanides, 2018c, when immiscible steady-state two-phase flows takes place within artificial 2D microfluidic networks, across different flow regimes. The general scope is to assess the applicability and/or universality of the aforementioned scaling function across NWP/WP/PM systems of different sizes and to examine the forensic character of the kernel function, i.e. the potential for revealing the interstitial flow structure.

The objective is two-fold:

(a) to examine the applicability of the proposed scaling on the basis of using typical regular core analysis measurements;

(b) to verify the existence, uniqueness and form of the locus of critical flow conditions, an inherent characteristic of such processes in terms of energy efficiency.

To do so we performed a systematic laboratory study of steady-state, two-phase flow in an artificial microfluidic pore network. Data were collected over a grid of specially selected flow conditions, spanning across 4 orders of magnitude on the capillary number, *Ca*, and up to 3 orders of magnitude on the flow rate ratio, *r*. With respect to (b), the existence of critical flow conditions (CFCs) has been already verified in an extensive review of published R/SCAL relative permeability diagrams (Valavanides *et al.*, 2016). Recently, the form of the locus of the CFCs proposed by Valavanides (2018b) was verified using a set of special core analysis relative permeability measurements (SCAL) performed on the same core and across a broad domain of flow conditions, *Ca* and *r* (Valavanides *et al.*, 2020). The present study is conceptually similar to that latter one. Nevertheless, as the general objective is to assess the applicability of the proposed generic form of flow-dependent relative permeability model on different types of pore networks, the current study addresses two-phase flows in an artificial pore network.

This article deploys in 3 sections. We start by providing the basic modeling assumptions for concurrent, immiscible, steady-state two-phase flows in porous media and present the basic structure of the proposed, flow-dependent relative permeability scaling. We continue with describing the systematic, steady-state, relative permeability measurements we have taken in a microfluidic network (Materials and Methods). Then, we present the results of the laboratory study examination and associated raw data calculations. Finally, we discuss "points of agreement/disagreement" between scaling predictions and actual measurements and we draw conclusions on the applicability of the proposed scaling or its potential exploitation in core analysis technology.

BASIC THEORETICAL BACKGROUND

Consider the simultaneous, one-dimensional concurrent flow of a non-wetting phase (NWP), and a wetting phase (WP). The variables pertaining to the NWP are indexed with n, whereas those pertaining to the WP are indexed with w. The compound flow is across a porous medium control surface, $\tilde{A}$, and induces flow rates equal to $\tilde{q}_n$ and $\tilde{q}_w$ respectively. Please keep in mind that, a tilde (~) is used to indicate a dimensional variable, no tilde indicates a dimensionless one. The phenomenological fractional flow Darcy relations that describe the steady-state, fully developed process, whereby the pressure gradient, $(\Delta\tilde{p}/\Delta\tilde{z})$, is common in both fluids (Valavanides, 2018b, Appendix I), are given by Eq. (1)

$$\tilde{U}_i = \frac{\tilde{q}_i}{\tilde{A}} = \frac{\tilde{k}}{\tilde{\mu}_i} k_{ri} \left(\frac{\Delta\tilde{p}}{\Delta\tilde{z}}\right) \quad , \qquad i = n, w \tag{1}$$

In one-dimensional flow under steady-state conditions, especially when the flow is fully developed, the common pressure gradient in both phases can be expressed in reduced form as

$$x = \frac{\Delta\tilde{p}/\Delta\tilde{z}}{(\Delta\tilde{p}/\Delta\tilde{z})^{1\Phi}} = \frac{\Delta\tilde{p}/\Delta\tilde{z}}{\tilde{\gamma}_{nw} Ca/k} = \frac{\Delta\tilde{p}}{\Delta\tilde{z}} \frac{\tilde{k}}{\tilde{\mu}_w \tilde{U}_w} = \frac{1}{k_{rw}} \tag{2}$$

where,

$(\Delta\tilde{p}/\Delta\tilde{z})^{1\Phi}$ is the pressure gradient corresponding to an equivalent saturated single-phase flow (1Φ) of the WP at the same superficial velocity $\tilde{U}_w$.

Ca is the capillary number, conventionally defined as

$$Ca = \tilde{\mu}_w \tilde{U}_w / \tilde{\gamma}_{nw} \tag{3}$$

$\tilde{\mu}_w$ is the viscosity of the WP, and

$\tilde{\gamma}_{nw}$ is the NWP/WP interfacial tension.

In Eq. (2) the actual pressure gradient is divided by the pressure gradient of an equivalent single-phase flow of the wetting phase with a superficial velocity equal to $\tilde{U}_w$, which is the 2nd component of the product. Note that, by definition, it is straightforward to verify that the reduced pressure gradient is essentially the inverse of the relative permeability of the WP [see far right side of Eq. (2)].

The set of superficial velocities in Eq. (1) may be appropriately reduced and replaced by a set of dimensionless variables, namely, the capillary number, *Ca*, as defined previously in Eq. (3), and the NWP/WP flow rate ratio,

$$r = \tilde{q}_n/\tilde{q}_w = \widetilde{U}_n/\widetilde{U}_w \tag{4}$$

At steady-state conditions when the flow is fully developed, i.e. there are either no end-effects or they can be considered to be negligible, the flow rate ratio, *r*, is equal to the mobility ratio, λ.

$$r = \frac{U_n}{U_w} \equiv \frac{1}{\kappa}\frac{k_{rn}}{k_{rw}} = \lambda \quad \Leftrightarrow \quad k_{rn} = \kappa r k_{rw} \tag{5}$$

where,

$$\kappa = \tilde{\mu}_n/\tilde{\mu}_w \tag{6}$$

is the NWP/WP bulk viscosity ratio.

The equivalence, expressed in the first part of Eq. (5), is a conjecture resulting from direct flow analysis (see Appendix I in Valavanides, 2018b) in case the flow is fully developed. Eq. (5) is very useful, as we may easily recover the r_i value pertaining to any pair i of measured $\{k_{rn}, k_{rw}\}_i$ values from a conventional (saturation dependent) relative permeability diagram. For a fully developed flow, we may also recover the value of a relative permeability (k_{rn} or k_{rw}) by knowing the values of the other relative permeability (k_{rw} or k_{rn}) and the flow rate ratio, *r*. Therefore, switching to the approach of flow-dependency may be readily applicable as all conventional relative permeability diagrams can still be used.

The conjecture that both fluids share a common pressure gradient, Eq. (1), is also based on experimental evidence. When measured values of flow rate ratio are plotted against calculated values of mobility ratio, they align on a straight line. Ample experimental evidence is provided in a recent work whereby ~180 relative permeability diagrams pertaining to steady-state conditions for a variety of NPW/WP/PM systems have been reviewed (Valavanides *et al.*, 2016). Because of the common pressure gradient [Eq. (1)] and the equivalence between flux ratio and mobility ratio, Eq. (5), relative permeability curves intersect at a fixed value of the flux ratio, the so-called relative permeability cross-over flux ratio value, r_x. The latter is inverse to the viscosity ratio,

$$r_x = 1/\kappa \tag{7}$$

as connoted by Eq. (5). This inherent characteristic of steady-state, fully developed flows is universally observed in all relative permeability vs flux ratio diagrams (Valavanides *et al.*, 2016; Valavanides, 2018b and Fig. 7). As we will see in the following, the same trend is generally also observed in the diagrams produced from the current study (**Fig. 7**). Therefore, the conjecture, eq. (5), proves to be quite trustworthy -to a certain extent.

In the line of the present work we will also analyze the results from an energy efficiency perspective. In this context, we will use the reduced, normalized measure of the energy efficiency of the process, considered as the flow rate of the NWP per unit of total hydraulic power spent, or equivalently, provided externally to the N/W/PM system (say by the "pumps"), to maintain two-phase flow -an essentially dissipative process- at any set of externally imposed flow conditions, *Ca* and *r*. The associated energy utilization factor, or energy efficiency index, f_{EU}, can be readily calculated in terms of macroscopic measurements (Valavanides, 2018b), as

$$f_{EU} = \frac{k_{rn}}{\kappa(r+1)} = \frac{r k_{rw}}{r+1} = \frac{r}{x(r+1)} \tag{8}$$

For every fixed value of the capillary number, *Ca*, there exists a single value of the flow rate ratio, *r**, for which the energy efficiency index, ${f_{EU}}^*$, attains a maximum value (Valavanides et al., 2016; Valavanides, 2018b). Moreover, for every NWP/WP/PM system, a unique locus of energy efficiency maxima is formed, $r^*(Ca)$. Flow conditions corresponding the $r^*(Ca)$ locus are called *critical flow conditions* (CFCs). Critical flow conditions can be measured and identified in a straightforward manner by typical relative permeability measurements. The efficiency index, f_{EU}, provides a strong flow analysis and characterization tool (Valavanides, 2018b).

Closing this passage, we need also to address the issue of selecting and using the flow rate ratio, *r*, instead of the fractional flow of the WP, f_w, as one of the two independent variables of the process – the other being the capillary number, *Ca*. In the core-analysis community the applicable standard is to refer to one of the fractional flows, by convention that of the WP, f_w. Switching between *r* and f_w (or f_n) is readily provided through the transformation $f_w = r/(1+r)$. Nevertheless, the use of the flow rate ratio, *r*, instead of the fractional flow, f_w, as independent variable, has the advantage of a more convenient description of the sought physical process, especially (or at least) around the critical flow conditions, whereby the identification of the critical flow rate ratio, $\log r^*(Ca)$, becomes more evident and obvious. The implications in using f_w, or f_n,, instead of r, are extensively discussed by Valavanides *et al.* (2016). As a general observation all $(f_{EU} \text{ vs } r)$ energy efficiency diagrams, show a more uniformly smooth trend when compared to the $(f_{EU} \text{ vs } f_w)$, irrespective of the particular values of the system parameters and flow conditions examined in that review.

2.1 Prediction of Steady-State Relative Permeabilities

The mechanistic model *DeProF* for immiscible, steady-state two-phase flow in pore networks may be used to predict the reduced macroscopic pressure gradient, x, given the flow conditions and system properties. The model is based on the concept of decomposition in prototype flows, hence the acronym *DeProF*. It takes in to account the pore-scale mechanisms and the sources of non-linearity caused by the motion of interfaces, as well as other complex, network-wide cooperative effects, to estimate -in a statistical sense- the conductivity of each class of pore unit cells. It implements effective medium theory with appropriate expressions for pore-to-macro scale consistency for NWP and WP mass transport, to derive an implicit algebraic relation invoking the macroscopic pressure gradient, the capillary number, Ca, the flow rate ratio, r, the viscosity ratio, κ, the dynamic advancing and receding contact angles, (θ_A, θ_R), and a set of parameters that describe the geometrical, topological and structural characteristics of the pore network, $\mathbf{x_{pm}}$ (Valavanides, 2018a)

Using the *DeProF* model, one can obtain the solution to the problem of steady-state two-phase flow in porous media in the form of the following transfer function,

$$x = x(Ca, r; \kappa, \theta_A, \theta_R, \boldsymbol{x_{pm}}) \quad (9)$$

Implementation of the *DeProF* model is possible when analytical expressions of the pore network geometry are plausible and general expressions for the pore network unit-cell conductivities can be calculated for all possible flow configurations. In general, this is not the case for real porous media, but only for a certain class of model pore networks with analytically tractable pore geometry. Yet, one can benefit by scanning entire domains of flow conditions at relatively short computational times and therefore get a systematic and consistent overview of the behavior of the flow across orders of magnitude of flow conditions. In that context, *DeProF* can be used as a virtual SCAL simulator implementing large cores with unbiased measurements, thanks to the absence of end-effects because of the "infinite" length of the virtual core.

Extensive simulations implementing the *DeProF* algorithm have been carried out in the past to derive maps that describe the dependence of the flow structure on the independent flow variables, namely the capillary number, Ca, and the flow rate ratio, r, or, equivalently, to the reduced, superficial velocities of NWP and WP (Valavanides, 2018a). The simulations span 5 orders of magnitude in Ca $(-9 \le \log Ca \le -4)$ and r $(-2 \le \log r \le 2)$ over sufficiently fine steps. Fluid systems with various viscosity ratios (9 in total), have been examined. Indicative *DeProF* model predictions of the reduced pressure gradient, x, are presented in **Fig. 1** for a typical NWP/WP/PM system with a viscosity ratio value of $\kappa = 1.5$. The diagrams furnish the projections of the $x_{ij}(Ca_i, r_j)$ predicted values on many constant-logCa_i planes in (a), and constant-logr_j planes in (b). In that context, markers are connected into iso-Ca and iso-r groups.

Referring to **Fig. 1**(a), at the high-end of the $\log r$ domain, all curves pertaining to constant-Ca values tend to bundle and align asymptotically to the straight (dashed) line. The corresponding functional form, Eq. (10), states that at sufficiently large Ca values the reduced pressure gradient becomes a linear function of the flow rate ratio, with the linearity coefficient being equal to the viscosity ratio, i.e. $\kappa = 1.5$.

$$\text{As } r \to \infty, \quad \log x = \log\kappa + \log r \quad \Leftrightarrow \quad x = \kappa r \quad (10)$$

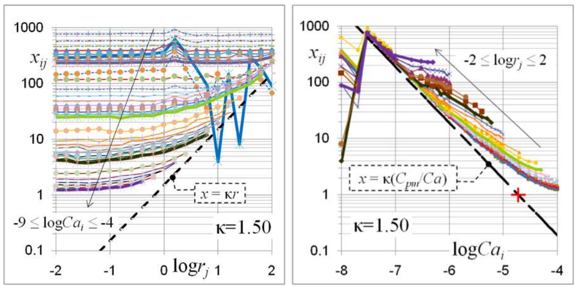

(a) (b)

Fig. 1 —Reduced pressure gradient values, *x*, for different values, (a) of the capillary number, Ca, and (b) of the flow rate ratio, *r*. Both diagrams pertain to a typical value of the viscosity ratio, κ=1.5

We may observe a similar trend in **Fig. 1**(b). At the low-end of the Ca domain, all iso-r curves tend to bundle and align asymptotically to a straight line, also illustrated with a dashed line. Now the functional form is given by the expression, up to a constant value, C_{pm}, associated to the NWP/WP/PM system (Valavanides, 2018c).

$$\log Ca \ll 0, \log x = \log\kappa - \log C_{pm} - \log Ca \\ \Leftrightarrow x = \kappa/(C_{pm} Ca) \tag{11}$$

2.2 Universal Scaling Form of Relative Permeabilities
Based on these simulations it was possible to derive a universal function that can describe the dependence of the *DeProF* model predicted values $x_{ij}(Ca_i, r_j)$ of the reduced pressure gradient for different values of the capillary number, *Ca*, and the flow rate ratio, *r*, by the universal scaling form (Valavanides, 2018c),

$$x(\log Ca, \log r) = A(\log Ca) + \kappa r \tag{12}$$

where the functional $A(\log Ca)$ may be determined by a fitting procedure. The set of (A_i, Ca_i) values is plotted on the diagram of **Fig. 2**. The cross-markers are lined-up against two straight line asymptotes; one with negative inclination and the other coinciding with the horizontal axis; these meet at an oblate angle.

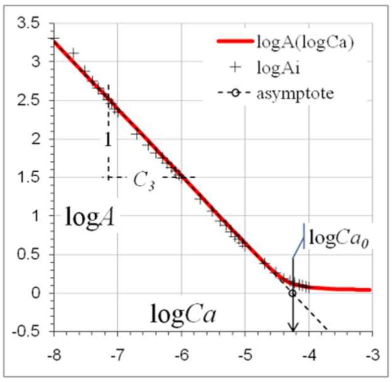

Fig. 2 — Kernel function values *A*, in terms of *Ca*. Cross-markers indicate values ($\log A_i$, $\log Ca_i$) of the kernel function used in Eq. (12) calculated to fit the *DeProF* predicted data, **Fig. 1**(b). These have been fitted by the thick red line, using Eq. (13). The black dashed line is an asymptote with gradient ($-1/C_3$)

We may fit to the set of $(\log Ca_i, \log A_i)$ values a function of the form,

$$\log Ca = \log Ca_0 + C_0/(\log A)^2 - C_3 \log A \tag{13}$$

where: $-1/C_3$ is the gradient of the inclined asymptote, and $\log Ca_0$ is the abscissa of the intersection of the two asymptotes. The coefficient C_0 is a measure of the overall distance (approach) to the two asymptotes (the higher this value, the greater the distance of the apex of the swarm of markers to the asymptotes' intersection). The values of coefficients pertaining to the particular NWP/WP/PM model system (examined in the *DeProF* simulations) are: $C_3 = 1.1474$, $\log Ca_0 = -4.3$, and $C_0 = 0.003$. The thick red line is the curve $\log A(\log Ca)$ that has been fitted to the raw data $\log A_i$ using Eq. (13). Please note, Eq. (13) is an implicit function of $\log A$ in terms of $\log Ca$. It can be solved analytically to provide an explicit expression $\log A(\log Ca/Ca_0\,; C_0, C_3)$.

Using the analytical expressions from Eqs. (12) and (13) with the aforementioned coefficient values, we may plot the reduced pressure gradient in terms of *Ca* and *r*, $x = x(Ca, r)$. Comparing the diagrams of **Fig. 3** to those in **Fig. 1**, we observe that the *DeProF* predicted values $x_{ij}(Ca_i, r_j)$ are recovered with great specificity, and that the trend at extreme flow conditions, maintains its physically-true characteristics (NWP flow is decoupled to the WP flow). Similar plots for other systems can be found in (Valavanides, 2018c).

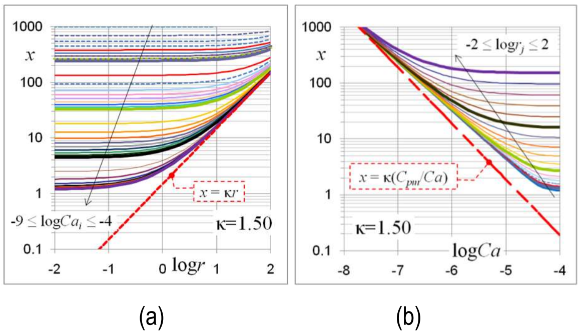

Fig. 3 — Plots of the reduced pressure gradient values, x, in terms of the flow conditions, *Ca* and *r*, based on Eqs. (12) and (13); (a) iso-*Ca* curves; (b) iso-*r* curves

In the present study we will repeat the procedure in a similar manner and try to recover an expression for the kernel function pertaining to the NWP/WP/PM system under consideration.

MATERIALS AND METHODS

The laboratory study presented here comprised the simultaneous, continuous, steady-state, co-current injections of two immiscible fluids within a specially prepared microfluidic network, for different flow conditions (152 runs in total organized in 13 groups of constant *Ca* values. The entire set of runs, spans across ~4 orders of magnitude on *Ca* and ~3 orders on *r* values.

3.1 Microfluidic Model and Fluids
A Poly-Di-Methyl-Siloxane (PDMS) micromodel was used as the pore network. The micromodel was produced in-house, following the principles of optical and soft

lithography (Xia and Whitesides, 1998). The pore structure of the micromodel is depicted in **Fig. 4**. The effective dimensions of the pore space are 10mm×20mm. The depth of the porous structure, is equal to 43 μm, and is constant throughout the entire pore space. The pore network is periodic in both principal orthogonal directions; it is made by tiling-up a basic network element in both directions; 3 periods along the longitudinal axis which is also the superficial flow direction, and 2 periods across the transverse axis. The pore size range is [75-250] μm, with a mean size equal to 180 μm. To network with this particular geometry is referenced as "Netwk22".

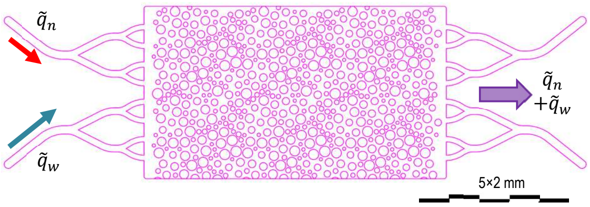

Fig. 4 — Plane section of the microfluidic PDMS network showing the pore structure of the porous medium. The physical dimensions (L×W×H) are 20mm×10mm×43μm. Circles correspond to the planar cross-sections of the PDMS cylinders of various diameters, connecting the two parallel plates confining the flow. The fluids are injected through the inlet micro-channeling at the left part of the network at predetermined fluxes, and the fluids are displaced outside of the pore network via the outlet micro-chanelling.

Based on the dimensions of the network the surface of the cross section (perpendicular to flow) is estimated at $\tilde{A} = 4.3 \times 10^{-7}\mathrm{m}^2$. The absolute permeability, taking in to account the inlet/outlet network, was measured at $\tilde{k} = 8.1 \times 10^{-1}\ \mathrm{m}^2$. The two immiscible fluids are injected through the inlet micro-channeling at the left part of the network and with predetermined fluxes, $\tilde{q}_n, \tilde{q}_w$; the immiscible flow exits through the outlet micro-channeling at the right.

Table 1 —Basic physicochemical properties of the fluids used in the study

Fluid	Density, $\tilde{\rho}$ [Kg/m^3]	Dynamic viscosity, $\tilde{\mu}$ [mPas]	Interfacial tension $\tilde{\gamma}_{nw}$ [N/m]
Fluorinert^{TM} FC-770 (WP)	1793	1.35	55×10^{-3}
Deionized Water + Dye (NWP)	1000	1.00	

The fluids used in the experiments were deionized water dyed with ink, as the non-wetting phase (NWP), and Fluorinert^{TM} FC-770, as the wetting phase (WP). The addition of the dye in water has practically no effect on its viscosity and density, something which was cross-checked by measurements. The basic properties of the fluids are presented in **Table 1**.

3.2 Experimental Set-up and Procedure

For the simultaneous injection of both fluids, at independent volumetric fluxes, two CETONI^{TM}, neMESYS 1000N, syringe pumps were used, one for each fluid. The syringe pumps were combined with a BASE120 module. With this set-up it was possible to inject the fluids at volumetric fluxes as low as a few microliters per minute (10^{-3}ml/min), to maintain a capillary-dominated flow regime, up to milliliters per minute (ml/min) to sustain viscosity-dominated flow regimes. The inlet pressure of each phase was measured with a variety of Elveflow^{TM} MPS sensors, depending on the values of the expected pressure build-up during the injection and the desirable /acceptable measurement accuracy. Both syringe pumps, and logging of the pressure readout values were controlled with QMixElements^{TM}.

In order to be able to assess whether or not the process has reached a steady state, the entire flow system was visualized using an open-air microscope; this was a modification of the one introduced by Karadimitriou *et al.*, 2013. The modification was such that just a single camera was used for the visualization of the entire network, instead of four. The camera used was a Basler^{TM} 5 Mpx, 23 fps, acA2440-20gm, monochrome camera. The purpose of visualizing the interstitial flow was for cross-checking between the structure of the flow, the read-outs from the pressure transducers, and the injected fluxes. There was no video recording but simple snapshot capturing. The frame rates used varied from 15 to 1 Hz, depending on the speed of the process, at a resolution around 8μm/pixel, which was adequate to observe pore-scale events.

Procedure followed for each experiment – With the term "experiment" we refer to a complete cycle of co-injecting the two phases, so that a constant value of the capillary number of the WP, Eq. (3), is maintained whereas the flux of the NWP is sequentially increased in successive steps. In that context a set of flow rate ratio values, r, spanning across 0.1 to 10 is administered for every fixed capillary number value, Ca. The domain of flow conditions in the entire set of experiments is depicted in **Fig. 5**.

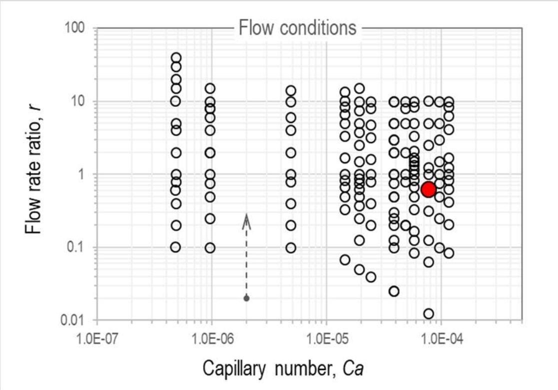

Fig. 5 — The domain of steady-state flow conditions examined in the study. Circular markers indicate values of the capillary number, *Ca*, and the flow rate ratio, *r*, examined per constant-*Ca* experiment. The arrow indicates the progressive increase of the flow rate of the NWP per experiment (at fixed *Ca*). The solid marker (in red color) identifies flow conditions pertaining to the time evolution diagram in **Fig. 6**. Each constant-*Ca* row is associated to corresponding diagram in **Fig. 7**.

The typical cycle in every experiment comprise the following interventions:

- The micromodel is initially saturated with the wetting phase, Fluorinert™. Then,
- Both phases are continuously injected into the microfluidic network; the WP is injected at a fixed volumetric flux in order to maintain a constant value of the capillary number, Ca, during the entire cycle of the experiment.
- The volumetric flux of the NWP starts at ~1/10 of the WP flux and it is increased in successive steps (about 9 to 12) to 10 times larger; the result is ~3 orders of magnitude in successive increments.
- After each step-up of the NPW flux, an adequate period of time is allowed for the flow to reach steady-state. Sampling and recording of the pressure values at the inlet port for each phase was set at rates between 0.5 and 10 Hz, depending on the flow conditions and the expected speed of events.
- As soon as the time-averaged pressure values showed signs of stabilization for both phases (kinetic stabilization), the entire microfluidic network was visually inspected in order to cross-check that the interstitial flow was also stabilized or any fluctuations showed some kind of sustainable, short-cycle periodicity. In most of the cases, a steady value for the pressures would come along with a stabilized flow, judging from visual inspection of the interstitial flow (changes in saturation, migration of menisci, other pore-scale phenomena). Occasionally, and most frequently for low volumetric fluxes of the NWP, we observed periodic fluctuations and/or oscillations over the pressure readouts for both phases, which would always be accompanied with snap-off events within the pores. In these cases, the system was left to oscillate for a few periods, so as to identify the characteristics of the oscillation, e.g. actual period and wavelength (see indicative case in **Fig. 6**). Our observations are in line with those reported in a recent work on interstitial flow fluctuations in natural cores (Rucker *et al.*, 2021).
- Following the establishment of steady-state conditions, the volumetric flux of the non-wetting phase is stepwise increased.
- After successive repeats with progressive stepwise increments of the volumetric flux of the NWP, the latter would have reached values 10 times the value of the WP, corresponding to a flow rate ratio value, $r = 10$. Then, the experiment for that particular constant Ca set stops.
- A new cycle (as described above) pertaining to a new Ca value is to be repeated. The system has then to be reconfigured to accommodate the next set of steady-state two-phase flows at a different constant Ca value (constant q_w value)

3.2 Data logging and management

For each run at constant $\tilde{q}_n$ and $\tilde{q}_w$ the values of flow rates and gauge pressures at the inlet ports for each phase, were sampled at predetermined rates and recorded. The recorded data were graphically plotted. End-point pressures were estimated from these plots by time averaging, over an adequate time length of sampling.

A typical procedure is depicted in the diagram in **Fig. 6**, on which the time evolution of the two flow rates and pressures at the inlet ports is displayed. Please note that, the time axis (horizontal) and the flux axis (vertical, right) are logarithmic whereas the pressure axis (vertical, left) is linear. Pressure values are indicated by markers; fluxes are indicated by lines. The endpoint pressure values were calculated by time averaging over a selected interval. The selected time interval is delimited by the two “×” markers. Delimiting this time interval for every examined flow set-up, (Ca, r), follows after identifying some form of stabilization in the corresponding pressure log diagram. Then, the average end-point pressures $\langle\tilde{P}_n\rangle, \langle\tilde{P}_w\rangle$, were automatically calculated by simple averaging over the selected time interval. These values, are displayed in **Table 2** columns (6) and (7) for the entire set of examined flows. The pressure gradients for the WP and the NWP are then readily calculated as

$$\left(\frac{\Delta\tilde{p}}{\Delta\tilde{z}}\right)_i = \frac{\langle\tilde{P}_i\rangle}{L}, \qquad i = n, w \qquad (14)$$

For example, in the flow set-up examined in **Fig. 6**, the endpoint pressures were averaged over the time interval $40s \leq t \leq 80s$, as indicated by the pair of cross markers (×) identifying the sampling interval on the WP and NWP pressure evolution plots.

The pair of pressure gradient values per phase, $\left\{\left(\frac{\Delta\tilde{p}}{\Delta\tilde{z}}\right)_n, \left(\frac{\Delta\tilde{p}}{\Delta\tilde{z}}\right)_w\right\}$, was then used to calculate the corresponding pair of relative permeability values for the NWP and WP, $\{k_{rn}, k_{rw}\}$, from Eq. (1).

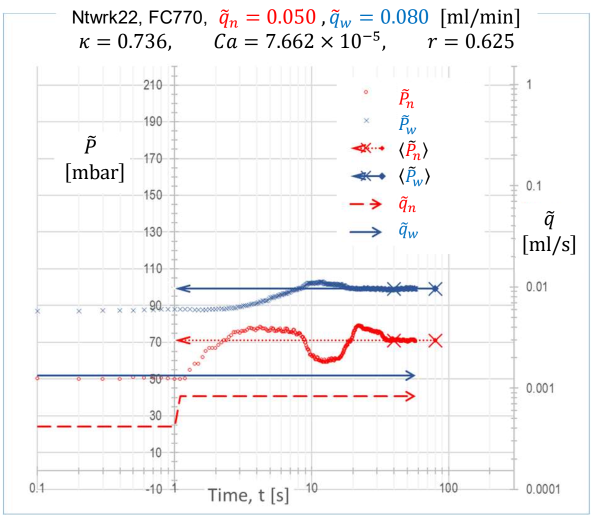

Fig. 6 — Time evolution of the inlet pressure for a typical co-injection of the two phases at predetermined volumetric flow rates. Compact line (blue, ▁▁) indicates the volumetric flow rate for the WP, $\tilde{q}_w$ dashed line (red, _ _) for the NWP, $\tilde{q}_n$ (the step indicates the imposed increase in volumetric flow rate succeeding the previous co-injection set-up). The time evolution of the measured pressure at the inlet port of the NWP is indicated by the small circle markers (red, ○); the pressure evolution at the WP inlet port is indicated by the small cross markers (blue, ×). The arrows indicate the pressure values reached when steady-state conditions settle-in. (see main text for details).

We need to stress here that we have considered the general condition that the flow may not be fully developed, therefore the NPW and WP pressure gradients are not necessarily equal. In such general condition, $(\Delta\tilde{p}/\Delta\tilde{z})_n \neq (\Delta\tilde{p}/\Delta\tilde{z})_w$, therefore

$$k_{rn} = \tilde{\mu}_n\tilde{U}_n \Big/ \left[\tilde{k}\left(\frac{\Delta\tilde{p}}{\Delta\tilde{z}}\right)_n\right] = \tilde{\mu}_n r \tilde{U}_w \Big/ \left[\tilde{k}\left(\frac{\Delta\tilde{p}}{\Delta\tilde{z}}\right)_n\right]$$
$$k_{rw} = \tilde{\mu}_w\tilde{U}_w \Big/ \left[\tilde{k}\left(\frac{\Delta\tilde{p}}{\Delta\tilde{z}}\right)_w\right] \qquad (15)$$

To test if the flow is fully-developed (at the end-point stage) we have calculated the mobility ratio, pertaining to the relative permeability values obtained from eq. (15)

$$\lambda = \frac{1}{\kappa}\frac{k_{rn}}{k_{rw}} \qquad (16)$$

After reviewing some preliminary results, we have decided to recalculate the energy efficiency values based on the mobility ratio values, Eq. (17), instead of the flow rate ratio values, r [ref. Eq. (8)], using the same structure as of the original /nominal expression,

$$f_{EU} = \frac{\lambda k_{rw}}{\lambda + 1} \qquad (17)$$

In that context it was more descriptive (in terms of the physics of the interstitial flow) to use the *kinetic* [Eq. (17)] rather than the *kinematic* [Eq. (8)] definition of the energy efficiency index.

At the end of the day, we have created an extensive database in the form of a look-up table with sets of calculated values corresponding to measurements for the entire ensemble of flow conditions. The entire set of calculated values of end-point pressures per (Ca, r) flow set-up is displayed in **Table 2**, at the end of the current article. Please note that the entire dataset is grouped to data sub-tables pertaining to constant Ca flows. The entire dataset of measurements, comprising the time evolution of the inlet gauge pressure for each phase and the corresponding fluxes, are available at the Data Repository of the University of Stuttgart (DaRUS), doi:10.18419/darus-2816.

RESULTS AND DISCUSSION

Pairs of NWP and WP relative permeability values $\{k_{rn}, k_{rw}\}_i$, were calculated using Eq. (15) for each measurement i $(i = 1, \ldots, 152)$. The collected relative permeability values were plotted against the corresponding values of the flow rate ratio, r_i, into diagrams pertaining to different constant-Ca experiments. These diagrams are presented in **Fig. 7**. The relative permeability values of the NWP and WP, k_{rn} and k_{rw}, are indicated by red squares and blue tringles respectively.

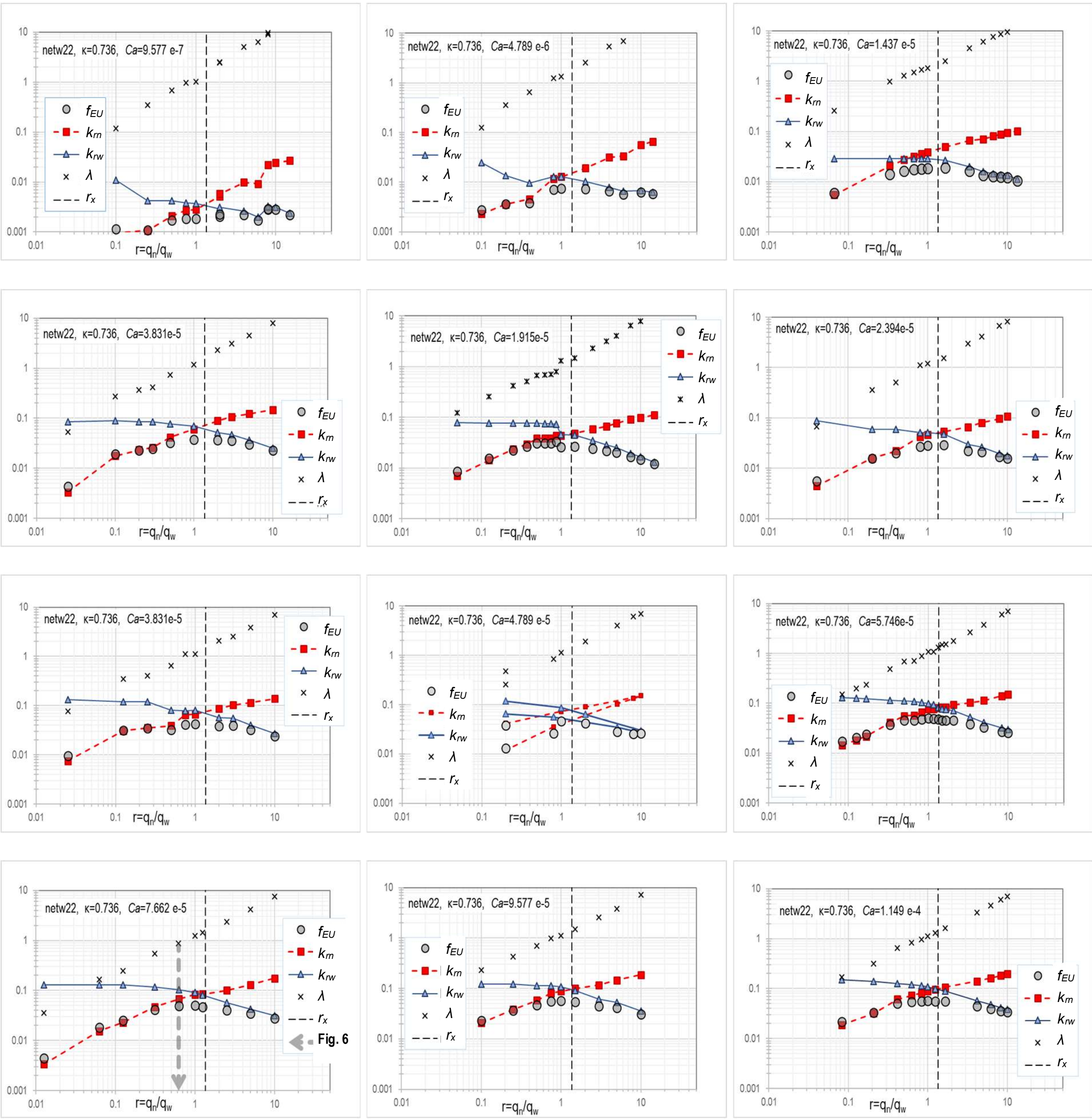

Fig. 7 — Relative permeability (■, ▲), energy efficiency (○), and mobility ratio (×) diagrams in the flow dependency format. Each diagram is associated to successive runs under constant *Ca* value. The straight, dashed, vertical lines indicate the theoretical value of the relative permeability cross-over flux ratio value, as predicted by Eq. (7). The smudged dashed thick line (grey) in the diagram at the bottom left corner, identifies calculated values pertaining to the time evolution of the inlet pressures in the diagram of **Fig. 6**. (also ref. in **Table 2.**)

In every constant-Ca diagram we have also plotted values of the mobility ratio, λ_i $(i = 1, \dots, 152)$, calculated using Eq. (16), as well as values of the energy efficiency $\{f_{EU}\}_i$ $(i = 1, \dots, 152)$, calculated using Eq. (17), against the values of the flux ratio, r_i. Please note that, the markers (×) indicating values of the mobility ratio, λ_i, against, r_i, are -in general- aligned along a straight line with a gradient equal to 1. In many cases, the two values are practically equal, i.e. $\lambda_i = r_i$. For those cases, the kinetic states of the interstitial flow structures, λ_i, are consistent to the externally imposed, kinematic constraints, r_i, and the corresponding flows should be fully developed. Yet, there are also many cases where, $\lambda_i \neq r_i$, albeit, on a logarithmic scale, $\log \lambda_i \sim \log r_i$. For those cases we expect that the kinetic state of the interstitial flow structure, λ_i, is not fully consistent to the corresponding, externally imposed, kinematic constraint, r_i, and the corresponding interstitial flow has not reached a fully developed structure.

In the same context, in many diagrams in **Fig. 7** pertaining to different constant-*Ca* experiments, the lines connecting the NWP and WP relative permeability markers intersect at the, so-called, relative permeability cross-over flux ratio value, $r_x = 1/\kappa$, as provided by Eq. (7). That value, is delineated in all diagrams in **Fig. 7**, by the vertical dashed line. For such cases, the conjecture of common pressure gradient in both fluids, and the associated relative permeability coupling between the NWP and WP, Eq. (5), are verified.

The hypothesis of common pressure gradient, is valid so long as the mobility ratio values are equal to the corresponding flux ratio values. That condition is reached when the externally imposed flow set-up matches the structure of the interstitial flow. End-effects are expected to be negligible for those particular sets of experiments.

Also, please note that, in every constant-*Ca* diagram in **Fig. 7**, energy efficiency, f_{EU} (○), increases with increasing flux ratio, it reaches a maximum value, then decreases. The trend is universal in all diagrams. These maximum energy efficiency values increase with increasing *Ca*. The flux ratio values, for which the energy efficiency attains a maximum value, i.e. the critical flow conditions, tend to decrease with increasing *Ca* values (compare diagrams from left to right, top to bottom). These findings are also presented more clearly in **Fig. 11**.

4.1 Flow dependency of relative permeability

We may now proceed with the validation of the proposed "flow dependent relative permeability scaling for steady-state two-phase flow" at least for a microfluidic network flow set-up, as the title clearly indicates.

We have calculated the reduced pressure gradient, $x = 1/k_{rw}$, i.e. the inverse of the relative permeability of the WP using Eq. (2). The entire set of *x* values is plotted in terms of the flow rate ratio, *r*, in **Fig. 8**, and in terms of the capillary number, *Ca*, in **Fig. 9**. In particular, Please note that, with increasing *r*, there is an obvious asymptotic trend in aligning to the dashed inclined line towards a virtually decoupled flow state, as provided by Eq. (10). The inclination of the dashed line is equal to the viscosity ratio, κ, as indicated by $\log x = \log \kappa + \log r \Leftrightarrow x = \kappa r$ [ref. Eq. (10)]. The trend for all iso-*Ca* groups of *x* values markers is similar to the trend observed in **Fig. 1**(a) from the *DeProF* model simulations pertaining to a virtual sandstone network model as well as the corresponding analytical fitting provided in **Fig. 3**(a). The same trend is observed in a similar diagram, pertaining to the lab study presented in Valavanides *et al.*, 2020. We need to remind here that this asymptote describes, or better, delineates, the domain of flow conditions whereby the compound flow resistance, attributed entirely to the bulk phase viscosities, is partitioned on complementary volume fraction rations (a.k.a. saturation). And that is the only case where relative permeabilities can be expressed in terms of saturation as "saturation-dependent rel-perms".

In **Fig. 8**, the reduced pressure gradient x_i −values ($i = 1, \ldots, 152$), are displayed in terms of log*r*, in groups of constant-*Ca* values.

In **Fig. 9**, the reduced pressure gradient x_i −values ($i = 1, \ldots, 152$), are displayed in terms of log*Ca*, lined up at constant-*Ca* groups. Within the same group, markers depict different values of the flow rate ratio, *r*. Note here: as we did not run all experiments on the same flow rate ratio values, it was not possible to group the *x*-values into *r*-classes.

Although not quite obvious, there is a tendency -a confluence- of the markers to converge and align -in an asymptotic manner- towards the inclined, dashed line. The trend is similar to that indicated in **Fig. 1**(b). Now the functional form of this asymptote is given by an expression, up to a constant value, C_{pm}, associated to the NWP/WP/PM system (Valavanides, 2018c) as described by Eq. (11). The particular line has a negative inclination equal in measure to the viscosity ratio, κ, as predetermined from flow analysis, as indicated by $\log x = \log C_{pm} - \log Ca$ for $\log Ca \ll 0$ [ref. Eq. (11)].

For the particular set of data displayed in **Fig. 9**, we have used an arbitrary, best-guess, constant value $C_{pm} = 3.9$ to pivot the line along the *Ca* axis. By increasing this value but keeping the negative inclination equal to κ, the line is parallelly transferred to the left, at lower *Ca* pivot points, and vice versa. To estimate a more precise C_{pm} value we need to have more data and, most importantly, the data should mostly pertain to capillarity dominated flows, i.e. to flows at lower *Ca* values. The recovery of the correct C_{pm} value for a certain system is essentially a "network-typing" procedure; that is because the value of C_{pm} is associated to the structure of the pore network.

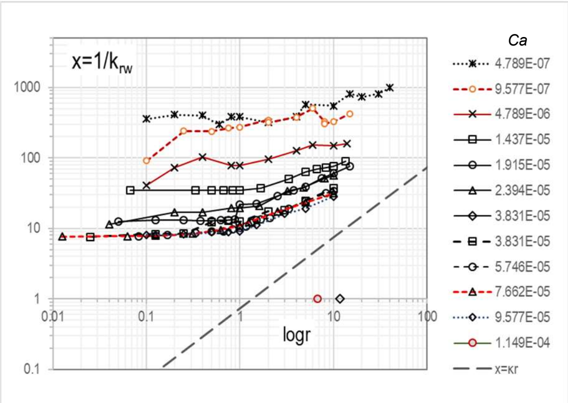

Fig. 8 — Reduced pressure gradient values, *x*, in terms of the flow rate ratio, *r*, grouped into constant Ca value.

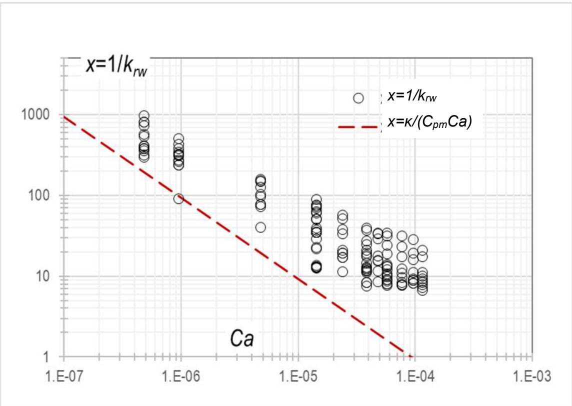

Fig. 9 — Reduced pressure gradient values, *x*, in terms of the capillary number, *Ca*.

4.2 Reveal of flow dependent rel-perm scaling

In order to describe the steady-state two-phase flow in the particular microfluidic system, in the form of the universal scaling function Eq. (12), we need to reveal the associated kernel function, $A(\log Ca)$. To this end we will implement a fitting procedure.

We start by the implicit definition of $A(\log Ca)$, through Eq. (12), to get

$$A(\log Ca) = x(\log Ca, \log r) - \kappa r \tag{18}$$

and then tap on the available reduced pressure gradient x_i −values $(i = 1, \dots, 152)$, collected from the experiments for different *r* values. Eq. (18) is recast to a data format

$$A_i = A(\log Ca_i) = x_{ij} - \kappa r_j \tag{19}$$

We plot the calculated A_i values in terms of Ca, in **Fig. 10**. The small black circles mark the kernel function values, A_i, aligned into constant-*Ca* groups. Average values of *A* per constant-*Ca* are marked with large red circles.

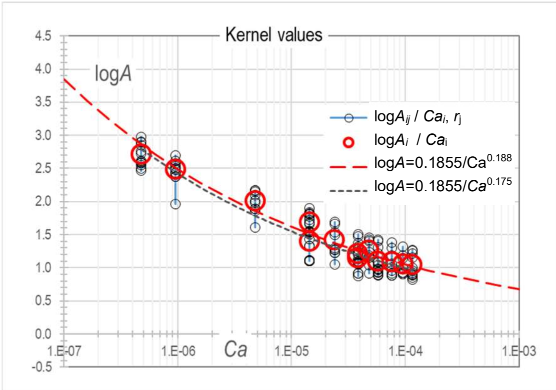

Fig. 10 — Small black circles mark the kernel function A_i values; these are aligned into constant-*Ca* groups. The short-dashed curve (in black) and the large red circles indicate average *A*-values per constant-*Ca*; the large-dashed curve (in red) show the corresponding power law trend curve fit.

The particular kernel function, Eq. (18), attributed to the system under examination, may be revealed by fitting an appropriate functional, e.g. a power law function, to the available data. We tried two fits. The first was implemented over the entire set of *A*-values; the fit is shown by the short-dashed black curve. The second fit was implemented over the average *A*-values per constant-*Ca* set; this is indicated by the large-dashed red curve. The curve is described by the simple power law expression

$$A(\log Ca) = 0.1855 Ca^{-0.188} \tag{20}$$

The power law fit indicates that $A(\log Ca)$ should asymptotically decay at very large *Ca* values ($A \xrightarrow{Ca \to \infty} 0$).

Yet this is something that needs further investigation and verification. There are some structural limitations in the particular type of PDMS microfluidic model pore networks: at relatively large Ca values the internal pressure increase -due to bulk viscosity induced resistances- deforms the geometry of the relatively soft PDMS matrix (Gervais *et al.*, 2006). That, on its turn, is expected to increase the effective porosity and absolute permeability. Consequently, that effect will eventually reduce the consistency -or direct compatibility- of any measured values across the entire domain of the flow conditions.

4.3 Energy efficiency and critical flow conditions

To reveal any latent systematic trends and eventually get a better image of the interstitial flow structure, we have further investigated the energy efficiency of the two-phase flow within the particular NWP/WP/PM system.

The diagrams in **Fig. 11** provide an overview of the energy efficiency analysis as it is implemented in this type of processes. In particular, the diagram in **Fig. 11**(a), displays the maximum values of energy efficiency attained at every constant-Ca experiment. The corresponding, critical flow conditions (CFCs), are displayed in the diagram in **Fig. 11**(b). They are all identified by observing the maximum values of the energy efficiency in the combined rel-perm and energy efficiency diagrams in **Fig. 7**, and looking-up values in **Table 2**.

We may recall here the definition of critical flow conditions as the conditions whereby the flowrate of the NWP per unit of hydraulic power necessary to maintain the compound flow takes maximum values. This is evaluated in an appropriately reduced form by the energy efficiency index, ref. Eq. (17). Diagrams in **Fig. 11** are similar to those furnished by Valavanides, 2018b, cf. figures 6 and 7, focusing on the expected universal layout of the locus of CFCs in such processes (two-phase flows in pore networks).

As said, the maximum energy efficiency values attained at every constant-Ca experiment are detected from trends in energy efficiency values observed in the diagrams in **Fig. 7**, taking also into account the explicit values of f_{EU} in column (13), **Table 2**. In that context, the f_{EU} maxima, each per constant-Ca experiment, are detected by

$$f^*_{EU,i} = f^*_{EU}(Ca_i) = \max_j\{f_{EU,ij,}, Ca_i\} \qquad (21)$$

Detected maximum energy efficiency values, at different capillary number values $\{f^*_{EU,i}, Ca_i\}$, for the $i = 1, \ldots, 13$ constant-Ca experiments are displayed in the diagram in **Fig. 11**(a). There is a remarkably smooth increase of the maximum energy efficiency values, f^*_{EU}, with increasing Ca.

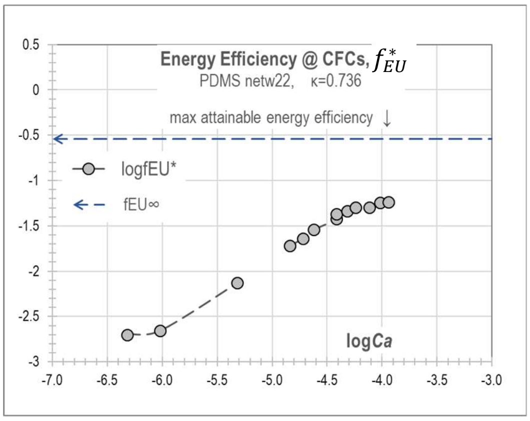

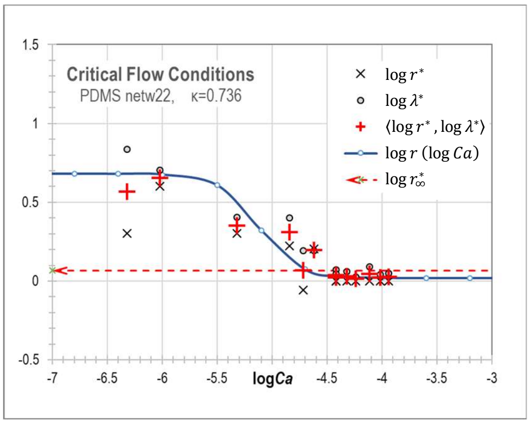

Fig. 11 — (a) Detected set of maximum energy efficiency values, at different capillary number values $\{f_{EU}{}^*_i, Ca_i\}$, ●, for the i=1,..,13 constant-Ca runs. **(b)** The corresponding critical flow rate ratio values, $\{r^*_i, Ca_i\}$, **×**, and mobility ratio values, $\{\lambda^*_i, Ca_i\}$, **o**, define the so-called Critical Flow Conditions; upright cross markers in red, **+**, indicate the mean value of the corresponding flowrate ratio and mobility ratio values.

It is worth noting that, depending on the flow conditions, the energy efficiency of the process may increase by 2 orders of magnitude. That is a quite important characteristic when designing the operation of similar processes. The values (markers) tend to reach a maximum value – the, so called, "ceiling of efficiency" (Valavanides, 2018b). Based on the energy efficiency analysis presented in this study, the maximum attainable value of the energy efficiency cannot exceed a value, dictated by the viscosity ratio of the system. This value is estimated to be equal to

$$f^*_{EU\infty} = \frac{1}{\left(1+\sqrt{\kappa}\right)^2} = \frac{1}{\left(1+\sqrt{0.732}\right)^2} = 0.2897 \qquad (22)$$

$$\Rightarrow \log f^*_{EU\infty} = -0.5380$$

We observe that the calculated values of the energy efficiency tend to have reached a maximum value significantly lower than the expected limit (the ceiling of efficiency). This discrepancy is attributed to a bias of the measured value of the absolute permeability of the microfluidic pore-network, due to the inlet and outlet tubing. Its nominal value is measured to be $\tilde{k} = 8.1 \times 10^{-11}\,\mathrm{m}^2$, whilst some assumptions are made for the permeability of the inlet and outlet tubing and micro channel flow distributors at the entry zone and collectors at the exit zone. Judging from the results, the aforementioned value overestimates the actual absolute permeability. We recall here that the energy efficiency is reduced by the power dissipation of an equivalent single-phase flow.

The corresponding critical flow rate ratio values, $\{r_i^*, Ca_i\}$, and mobility ratio values, $\{\lambda_i^*, Ca_i\}$. are plotted in terms of logCa in the diagram in **Fig. 11**(b). The corresponding markers define the so-called locus of Critical Flow Conditions (or, CFC locus).

We may observe a discrepancy between the mobility ratio and flowrate ratio values at CFCs; the discrepancy is pronounced at the lower part of the *Ca* domain, i.e. at capillary dominated flow regimes, while it becomes insignificant at the high *Ca* domain where bulk viscosity prevails and the effect of menisci is practically negligible. The observed discrepancy is attributed to the procedure in detecting the CFCs and the associated mobility and flowrate ratio values: From energy efficiency values calculated on a mobility ratio basis [(ref. Eq. (17)], the maximum per constant-*Ca* experiment, $f^*_{EU}|_{Ca}$, is detected by referring to column (13), **Table 2** and the corresponding flowrate ratio value $r^*|_{Ca}$, is traced by looking-up in column (5), **Table 2**. Focusing on the low-*Ca* regime, on the upper left diagrams in **Fig. 7**, we may observe a significant discrepancy between the mobility ratio and the flowrate ratio, manifested as a failure of the $\{r, \lambda\}$ markers to perfectly align to the $r = \lambda$ straight line. The source of this discrepancy can be traced-back to the end-effects that are induced by the relatively stronger role of the menisci – when compared to the effects of the bulk viscosity.

The detected CFCs show a tendency to line-up on an S-shaped curve. A similar trend is manifested in the study deployed by Valavanides *et al.*, 2020, and it is supported by inferences derived by Valavanides (2018b) based on energy efficiency analysis. This tendency is a little bit fuzzy in the low-*Ca* regime. To overcome this fuzziness, we have defined the log-average values of $\{r, \lambda\}$ per CFC, $\log\hat{r}^* = \langle \log r^*, \log \lambda^* \rangle$, calculated as

$$\log\hat{r}^* = \frac{\log r^*}{2} + \frac{\log \lambda^*}{2} \quad \Leftrightarrow \quad \hat{r}^* = \sqrt{r^* \lambda^*} \qquad (23)$$

These values are also plotted in the CFS diagram, **Fig. 11**(b), as indicated by the upright cross markers (in red). Now the trend in the CFCs markers becomes clearer that it is of an S-shape curve. This is consistent to the $r^*(Ca)$ shape of the CFC locus on the universal energy efficiency map illustrated in Valavanides, 2018b (cf. reference Figure 6 and 7).

The dashed red horizontal line indicates the nominal value of the critical flow rate ratio for pure viscous flow conditions (as *Ca*→∞). Given the viscosity ratio value of the examined NPW/WP system, $\kappa = 0.732$, this CFC nominal value for pure viscous flow conditions is estimated to be $r^*_\infty = 1/\sqrt{\kappa} = 1/\sqrt{0.732} = 1.1656$ ($\log r^*_\infty = 0.06656$). This value is indicated by the dashed straight line (in red color) in the diagram **Fig. 11**b. The actual value attained within the lower part of the S-shape form, pertaining to larger *Ca*-values, indicates an asymptotic trend (*Ca*→∞) remarkably close to the aforementioned theoretically predicted value.

The trend is indicated by fitting an S-curve, to the available CFC data points. The fitted S-curve is given by the following expression

$$\log r^*(\log Ca) = \\ = 0.33\tanh[2.85(\log Ca + 5.13)] + 0.35 \qquad (24)$$

CONCLUSIONS

We have assessed /validated the specificity and applicability of a new flow-dependent relative permeability scaling law that takes explicitly into account capillarity effects. Flow dependency is associated to the flow intensities of the NWP and WP or, equivalently, to the capillary number of the WP, *Ca*, and the NWP/WP flow rate ratio, *r*. The proposed scaling is built around a kernel function, log*A*(log*Ca*), that provides a bridge between the decoupled character of the flow at the two extreme flow regimes (low-*Ca*/low-*r* to high-*Ca*/high-*r* flows). The validation was based on a set of 13 experiments of steady-state two-phase flow through a PDMS microfluidic pore-network. Each experiment was run at constant *Ca* for the WP for a variety of volumetric flux ratio values. The experiments covered different flow conditions, spanning across 4 orders of magnitude in *Ca* and 3 orders of magnitude in *r*, over an almost rectangular domain in *Ca*×*r*. The system of fluids had a viscosity ratio of ~0.7 and showed intermediate wettability against the PDMS network matrix.

The results suggest that it is possible to derive and implement universal, true-to-mechanism functions describing correctly the flow-dependency of relative permeabilities. The critical step here is to infer and then data-fit an appropriate form of the kernel function, log*A*(log*Ca*). The kernel function is associated with the complex rheologic character of the NWP/WP/PM system manifesting itself across the entire *Ca* domain.

The specificity /applicability of the proposed scaling is substantial and deserves further investigation, mainly towards understanding the universal structure of the kernel function log*A*(log*Ca*). Because of the structure of the scaling, Eq. (12), the mode of decaying of log*A* at high-*Ca* regimes, strongly depends on the physicochemical properties of the NWP/WP/PM system, e.g. wettability. The universal, critical property of the kernel function should be a monotonous decay at the high-*Ca* regime.

By implementing the proposed flow-dependency analysis it was possible to gain a consistent and well-structured view of the process over the domain of examined flow conditions. The calculated values of reduced quantities (reduced pressure gradient, kernel function) show a consistent dependency on flow conditions and can be used to reveal the interstitial flow mechanisms.

Reviewing the present work in terms of reaching its objectives, we may conclude:

(a) Implementation of the proposed scaling is possible using rather simple and well-known interventions, typical of regular core analysis protocols; moreover, it was possible to rely on superficial measurements only, i.e. flow rates of the two phases, pressure drop across the core length, interfacial tension, absolute permeability.

(b) We have tested the hypothesis of fully developed flow conditions. In that context we have NOT considered *a priori* equal pressure gradients across the pore network. Instead, we have based our post-analysis on considering decoupled pressure drops across the flow of each phase. It turned out that equality of pressure gradients is a testable hypothesis; the test is easy to implement as we have shown in the current study.

(c) The existence, uniqueness and form of the locus of critical flow conditions (CFCs), $r^*(Ca)$, was confirmed. The S-shape type, confined between two asymptotic lines, $r = r_0^*$ and $r = r_\infty^*$, as proposed in Valavanides, 2018b is also confirmed. Differences between nominal, expected, and actual, measured values, of r_∞^*, and $f_{EU\infty}^*$, are also justified. In order to reveal the S-shaping in greater detail, the flow conditions should be finely scanned /tuned in proximity to the transition zone of the CFC locus. i.e. the transition part of the S-curve.

(d) By implementing the proposed scaling and considering the underlying mechanisms of the interstitial flows, we can explain the flow behavior by referring to the macroscopic measurements. That was possible by examining the structure of the WP relative permeability, k_{rw}, and of the kernel function *A*, without any need to examine the flow at the pore scale using sophisticated equipment. Therefore, the proposed scaling could potentially serve as an additional tool for quality assessment of measurements (R/SCAL forensics).

Based on the results of this preliminary assessment, it would make sense to consider designing and deploying a systematic laboratory study to investigate and reveal the effects of wettability, pore network structure, core size, etc. on the form of $A(\log Ca)$. We intend to extend the experimental study with model pore networks of different geometries. The scope would be to further examine if the proposed analysis and applicable methodology associated to the proposed flow dependency scaling of relative permeabilities, can be implemented to address potential improvements of the R/SCAL protocols and in rock typing associated to interstitial flow; also, to develop more robust and accurate macroscopic scale models.

ACKNOWLEDGEMENTS

M.S. Valavanides would like to thank

1. the German Academic Exchange Service (DAAD - 5752335 Research Stays for University Academics and Scientists, 2021)

2. the Society of Petrophysicists and Well Log Analysts (SPWLA Foundation Board, 2021 award)
3. the University of West Attica, as well as the Erasmus+ programme, project -2020-1-EL01-KA103-077837

N. Karadimitriou and H. Steeb would like to thank

1. the Deutsche Forschungsgemeinschaft (DFG) for supporting this work by funding EXC2075-390740016 under Germany's Excellence Strategy, as well as
2. the DFG for supporting this work by funding of Sonderforschungsbereich (SFB) 1313 project 327154368.

The datasets for boundary phase pressures and the corresponding fluxes are available at the Data Repository of the University of Stuttgart (DaRUS), DOI: 10.18419/darus-2816.

NOMENCLATURE

Abbreviations

CFC = critical flow conditions
NPW = non-wetting phase
PDMS = Poly-Di-Methyl-Siloxane
PM = porous medium
REV = representative elementary volume
R/SCAL = Regular/Special Core Analysis Laboratory
WP = wetting phase

Symbols

Latin
A = kernel function, 1
$\tilde{A}$ = cross-sectional area of the pore network perpendicular to the flow, m^2
Ca = Capillary number (conventional definition), 1
f_{EU} = energy efficiency, 1
k_{rn} = relative permeability of nonwetting phase, 1
k_{rw} = relative permeability of wetting phase, 1
$\tilde{U}$ = superficial velocity, m/s
$\tilde{k}$ = absolute permeability, m^2
$\tilde{p}, \tilde{P}$ = pressure, N/m^2
$\tilde{q}$ = volumetric flow rate, m^3/s
x = reduced pressure gradient, 1
Greek
$\tilde{\gamma}_{nw}$ = interphasial tension, N/m
Δ = difference
dynamic advancing and receding contact angles,
θ = dynamic contact angle (meniscus to pore wall), 1
κ = (nonwetting/wetting) viscosity ratio, 1
λ = (nonwetting/wetting) mobility ratio, 1
$\tilde{\mu}$ = dynamic viscosity, Pa s

REFERENCES

Armstrong, R.T., McClure, J.E., Berrill, M.A., Rücker, M., Schlüter, S., and Berg, S., 2016, Beyond Darcy's law: The Role of Phase Topology and Ganglion Dynamics for Two-Fluid Flow., *Phys. Rev. E*, **94**, 043113. DOI: 10.1103/PhysRevE.94.043113.

Aursjo, O., Erpelding, M., Tallakstad, K.T., Flekkøy, E.G., Hansen, A., and Maloy, K.J., 2014, Film Flow Dominated Simultaneous Flow of two Viscous Incompressible Fluids Through a Porous Medium., *Frontiers in Physics*, **2**(63), 1-9. DOI: 10.3389/fphy.2014.00063.

Datta, S.S., Ramakrishnan, T.S., and Weitz, D.A., 2014, Mobilization of a Trapped Non-wetting Fluid From a Three Dimensional Porous Medium., *Phys. Fluids*, **26**. DOI: 10.1063/1.4866641.

Georgiadis, A., Berg, S., Makurat, A., Maitland, G., and Ott, H, 2013, Pore-Scale Micro-Computed-Tomography Imaging: Nonwetting-Phase Cluster-Size Distribution During Drainage and Imbibition., *Phys. Rev. E*, **88**(033002), 1-9. DOI: 10.1103/PhysRevE.88.033 002.

Gervais, T., El-Ali, J., Gunther, A., and Jensen, K. F., 2006, Flow-induced deformation of shallow microfluidic channels., *Lab on a Chip*, **6**, 500–507. DOI: 10.1039/b513524a

Guillen V.R., Carvalho, M.S., and Alvarado, V., 2012, Pore Scale and Macroscopic Displacement Mechanisms in Emulsion Flooding., *Transport in Porous Media*, **94**, 197–206. DOI: 10.1007/s11242-012-9997-9.

Hinkley, R.E., Dias, M.M. and Payatakes, A.C. 1987, On the Motion of oil Ganglia in Porous Media, *Physico-Chemical Hydrodynamics*, **8**(2), 185-211. No DOI found.

Karadimitriou, N. K., M. Musterd, P. J. Kleingeld, M. T. Kreutzer, S. M. Hassanizadeh, and V. Joekar-Niasar, 2013, On the fabrication of PDMS micromodels by rapid prototyping, and their use in two-phase flow studies., *Water Resources Research*, **49**, 2056–2067. DOI: 10.1002/wrcr.20196.

Oughanem, R., Youssef, S., Bauer, D., Peysson, Y., Maire, E., and Vizika, O., 2015, A Multi-Scale Investigation of Pore Structure Impact on the Mobilization of Trapped Oil by Surfactant Injection., *Transport in Porous Media*, **109**, 673-692. DOI: 10.1007/s11242-015-0542-5.

Rücker, M., Georgiadis, A., Armstrong, R.T., Ott, H., Brussee, N., van der Linde, H., Simon, L., Enzmann, F., Kersten, M. and Berg, S., 2021, The Origin of Non-thermal Fluctuations in Multiphase Flow in Porous Media., *Frontiers in Water*, **3**(671399), 1-25. DOI: 10.3389/frwa.2021.671399

Sinha, S. Bender, A.T., Danczyk, M., Keepseagle, K., Prather, C.A., Bray, J.M., Thrane, L.W., Seymour, J.D., Codd, S.I., and Hansen, A., 2017, Effective Rheology of Two-Phase Flow in Three-Dimensional Porous Media: Experiment and Simulation., *Transport in Porous Media*, **119**, 77-94. DOI: 10.1007/s11242-017-0874-4.

Tallakstad, K.T., Knudsen, H.A., Ramstad, T., Løvoll, G., Maløy, K.J., Toussaint, R., and Flekkøy, E.G., 2009, Steady-State Two-Phase Flow in Porous Media: Statistics and Transport Properties., *Physical Review Letters* 102 074502, 1-4. DOI: 10.1103/PhysRevLett.102.074502.

Tsakiroglou, C.D., Avraam, D.G., and Payatakes, A.C., 2007, Transient and Steady-State Relative Permeabilities from Two-Phase Flow Experiments in Planar Pore Networks., *Advances in Water Resources*, **30**, 1981–1992. DOI: 10.1016/j.advwatres.2007.04.002.

Tsakiroglou, C.D. Aggelopoulos, C.A., Terzi, K., Avraam, D.G., and Valavanides, M.S., 2015, Steady-State Two-Phase Relative Permeability Functions of Porous Media: A Revisit., *International Journal of Multiphase Flow*, **73**, 34–42. DOI: 10.1016/j.ijmultiphaseflow.2015.03.001.

Valavanides, M.S., 2018a, Oil Fragmentation, Interfacial Surface Transport and Flow Structure Maps for Two-Phase Flow in Model Pore Networks. Predictions Based on Extensive, DeProF Model Simulations., *Oil & Gas Science and Technology - Rev. IFP Energies Nouvelles*, **73**(6), 1-36. DOI: 10.2516/ogst/2017033

Valavanides, M.S., 2018b, Review of Steady-State Two-Phase Flow in Porous Media: Independent Variables, Universal Energy Efficiency Map, Critical Flow Conditions, Effective Characterization of Flow and Pore Network., *Transport in Porous Media*, **123**(1), 42-99. DOI: 10.1007/s11242-018-1026-1.

Valavanides, M.S., 2018c, True to mechanism, flow dependent relative permeability scaling functional form for steady-state 2-phase flows in p.m.., paper SCA2018-066, *Proceedings of the International Symposium of the Society of Core Analysts*, Trondheim, Norway, 27-30 August. http://users.uniwa.gr/marval/publ/Valavanides_SCA2018_066.pdf

Valavanides, M.S., Totaj, E., and Tsokopoulos, M., 2016, Energy Efficiency Characteristics in Steady-State Relative Permeability Diagrams of Two-Phase flow in Porous Media", Journal of Petroleum Science and Engineering, **147**, 181-201, DOI: 10.1016/j.petrol.2016.04.039

Valavanides, M.S., Mascle, M., Youssef, S., and Vizika, O., 2020, Steady-State Two-Phase Flow in Porous Media: Laboratory Validation of Flow Dependent Relative Permeability Scaling., *E3S Web of Conferences*, **146**(03002), The International Symposium of the Society of Core Analysts, SCA2019. DOI: 10.1051/e3sconf/202014603002

Xia, Y., and Whitesides, G.M., 1998, Soft Lithography., *Annual Review of Materials Science*, **28**, 153-184. DOI: 10.1146/annurev.matsci.28.1.153.

ABOUT THE AUTHORS

Marios Valavanides - is Professor of Hydraulics and Porous Media Flow at the Department of Civil Engineering, University of West Attica (UniWA), Athens, Greece. His research focuses on modeling of two-phase flow in porous media; he is the main contributor in the development of the DeProF theoretical framework – build around the flowrate dependency of two-phase flow in porous media (http://users.uniwa.gr/marval/ImproDeProF.html).

Nikolaos Karadimitriou, PhD is Post-Doctoral Research Associate at the Institute of Applied Mechanics, Faculty of Civil and Environmental Engineering, University of Stuttgart, Germany. He has extended experience and expertise in designing and manufacturing artificial porous media with desired flow patterns, as well as physical and chemical properties. His research focuses primarily on experimental two-phase flow and transport, either from a fundamental research scope, or application-driven. He has developed three complete microfluidic labs in three different countries and universities. He also has extensive experience in the use and development of various microscopy techniques, including optical, fluorescence, confocal and thermal.

Holger Steeb - is full Professor (W3) and Director of the Institute of Applied Mechanics, Faculty of Civil and Environmental Engineering and Fellow of SC SimTech, University of Stuttgart, Germany. Holger Steeb and his group investigated hydromechanical coupling of porous media theoretically, numerically and experimentally on various scales. This involves small scale, i.e. Direct Numerical Simulations (DNS) on the pore scale, e.g. based on light- or X-ray micro-CT images (incl. in-situ hydro-mechanical experiments), as well as macro (continuum) scale investigations. Further, Holger Steeb established the “Porous Media Lab” at the University of Stuttgart fostering micro-fluidic experimental investigations of multi-phase flow.

Table 2 — The raw data values measured or calculated in the course of the present study. The second raw on the heading refer the equation used to calculate the values.

1	2	3	4	5	6	7	8	9	10	11	12	13
$\tilde{q}_n$	$\tilde{q}_w$	$\tilde{U}_w$	$\boldsymbol{Ca}$	$\boldsymbol{r}$	$\langle\tilde{P}_n\rangle$	$\langle\tilde{P}_w\rangle$	$\langle\frac{d\tilde{P}_n}{d\tilde{z}}\rangle$	$\langle\frac{d\tilde{P}_w}{d\tilde{z}}\rangle$	k_{rn}	k_{rw}	λ	f_{EU}
		Eq. (1)	Eq. (3)	Eq.(4)			Eq. (14)		Eq.(15)	Eq.(15)	Eq.(16)	Eq.(17)
[ml/min]	[ml/min]	[m/s]	[-]	[-]	[mbar]	[mbar]	[N/m]	[N/m]	[-]	[-]	[-]	[-]
0.00005	**0.0005**	1.94	**4.789**	0.10	3.047	23.093	1.523E+04	1.155E+05	0.0016	0.0028	0.758	0.0012
0.0001		$\times10^{-5}$	$\boldsymbol{\times10^{-7}}$	0.20	3.885	26.663	1.942E+04	1.333E+05	0.0025	0.0024	1.373	0.0014
0.0002				0.40	9.456	26.097	4.728E+04	1.305E+05	0.0020	0.0025	1.104	0.0013
0.0003				0.60	7.618	19.317	3.809E+04	9.658E+04	0.0038	0.0034	1.521	0.0020
0.0004				0.80	10.636	24.927	5.318E+04	1.246E+05	0.0036	0.0026	1.875	0.0017
0.0005				1.00	12.301	24.752	6.151E+04	1.238E+05	0.0039	0.0026	2.012	0.0018
0.0010				2.00	8.850	20.592	4.425E+04	1.030E+05	0.0108	0.0032	4.654	0.0026
0.0020				4.00	10.926	24.860	5.463E+04	1.243E+05	0.0175	0.0026	9.101	0.0024
0.0025				5.00	27.167	37.382	1.358E+05	1.869E+05	0.0088	0.0017	6.880	0.0015
0.0050				10.00	26.048	35.363	1.302E+05	1.768E+05	0.0184	0.0018	13.576	0.0017
0.0075				15.00	32.429	52.755	1.621E+05	2.638E+05	0.0221	0.0012	24.402	0.0012
0.0100				20.00	36.484	47.253	1.824E+05	2.363E+05	0.0262	0.0014	25.903	0.0013
0.0150				30.00	52.456	52.607	2.623E+05	2.630E+05	0.0274	0.0012	30.086	0.0012
0.0200				40.00	49.739	63.906	2.487E+05	3.195E+05	0.0385	0.0010	51.394	0.0010
0.00010	**0.001**	3.876	**9.577**	0.10	10.194	11.882	5.097E+04	5.941E+04	0.0009	0.0109	0.117	0.0011
0.00025		$\times10^{-5}$	$\boldsymbol{\times10^{-7}}$	0.25	22.375	31.114	1.119E+05	1.556E+05	0.0011	0.0042	0.348	0.0011
0.00050				0.50	22.944	30.879	1.147E+05	1.544E+05	0.0021	0.0042	0.673	0.0017
0.00075				0.75	26.508	34.476	1.325E+05	1.724E+05	0.0027	0.0038	0.975	0.0019
0.001				1.00	34.325	35.340	1.716E+05	1.767E+05	0.0028	0.0037	1.030	0.0019
0.002				2.00	36.810	44.825	1.840E+05	2.241E+05	0.0052	0.0029	2.436	0.0021
0.002				2.00	33.157	41.295	1.658E+05	2.065E+05	0.0058	0.0031	2.491	0.0022
0.004				4.00	38.910	49.098	1.946E+05	2.455E+05	0.0098	0.0026	5.047	0.0022
0.006				6.00	62.162	65.911	3.108E+05	3.296E+05	0.0092	0.0020	6.362	0.0017
0.008				8.00	34.605	42.031	1.730E+05	2.102E+05	0.0221	0.0031	9.717	0.0028
0.008				8.00	35.198	39.990	1.760E+05	2.000E+05	0.0218	0.0033	9.089	0.0029
0.010				10.00	39.320	42.123	1.966E+05	2.106E+05	0.0243	0.0031	10.713	0.0028
0.015				15.00	53.364	55.457	2.668E+05	2.773E+05	0.0269	0.0023	15.588	0.0022
0.0005	**0.005**	1.938	**4.789**	0.10	20.841	26.362	1.042E+05	1.318E+05	0.0023	0.0247	0.126	0.0028
0.0010		$\times10^{-4}$	$\boldsymbol{\times10^{-6}}$	0.20	26.664	47.191	1.333E+05	2.360E+05	0.0036	0.0138	0.354	0.0036
0.0020				0.40	41.579	67.162	2.079E+05	3.358E+05	0.0046	0.0097	0.646	0.0038
0.0040				0.80	32.285	50.396	1.614E+05	2.520E+05	0.0119	0.0129	1.249	0.0072
0.0050				1.00	37.211	50.223	1.861E+05	2.511E+05	0.0129	0.0129	1.350	0.0074
0.0100				2.00	49.691	62.979	2.485E+05	3.149E+05	0.0193	0.0103	2.535	0.0074
0.0200				4.00	60.416	82.081	3.021E+05	4.104E+05	0.0317	0.0079	5.434	0.0067
0.0300				6.00	85.575	99.445	4.279E+05	4.972E+05	0.0336	0.0065	6.972	0.0057
0.0500				10.00	85.553	95.964	4.278E+05	4.798E+05	0.0559	0.0068	11.217	0.0062
0.0700				14.00	101.958	102.830	5.098E+05	5.142E+05	0.0657	0.0063	14.120	0.0059
0.0010	**0.015**	5.81	**1.437**	0.07	17.540	67.767	8.770E+04	3.388E+05	0.0055	0.0288	0.258	0.0059
0.0050		$\times10^{-4}$	$\boldsymbol{\times10^{-5}}$	0.33	22.978	68.105	1.149E+05	3.405E+05	0.0208	0.0286	0.988	0.0142
0.0075				0.50	26.247	67.867	1.312E+05	3.393E+05	0.0273	0.0287	1.293	0.0162
0.0100				0.67	29.847	67.646	1.492E+05	3.382E+05	0.0321	0.0288	1.511	0.0174
0.0125				0.83	33.026	67.657	1.651E+05	3.383E+05	0.0362	0.0288	1.707	0.0182
0.0150				1.00	36.885	68.026	1.844E+05	3.401E+05	0.0389	0.0287	1.844	0.0186
0.0250				1.67	48.411	72.963	2.421E+05	3.648E+05	0.0494	0.0267	2.512	0.0191
0.0500				3.33	72.020	98.813	3.601E+05	4.941E+05	0.0664	0.0197	4.573	0.0162
0.0750				5.00	101.355	123.762	5.068E+05	6.188E+05	0.0708	0.0158	6.105	0.0135
0.1000				6.67	118.992	135.779	5.950E+05	6.789E+05	0.0804	0.0144	7.607	0.0127
0.1250				8.33	135.794	141.265	6.790E+05	7.063E+05	0.0881	0.0138	8.669	0.0124
0.1500				10.00	153.254	147.290	7.663E+05	7.365E+05	0.0937	0.0132	9.611	0.0120
0.2000				13.33	187.359	174.614	9.368E+05	8.731E+05	0.1022	0.0112	12.426	0.0103
0.0010	**0.02**	7.751	**1.915**	0.05	13.449	32.642	6.724E+04	1.632E+05	0.0071	0.0797	0.121	0.0086
0.0025				0.13	16.622	34.057	8.311E+04	1.703E+05	0.0144	0.0764	0.256	0.0156

1	2	3	4	5	6	7	8	9	10	11	12	13
$\tilde{q}_n$	$\tilde{q}_w$	$\tilde{U}_w$	$\boldsymbol{Ca}$	$\boldsymbol{r}$	$\langle \tilde{P}_n \rangle$	$\langle \tilde{P}_w \rangle$	$\langle \frac{d\tilde{P}_n}{d\tilde{z}} \rangle$	$\langle \frac{d\tilde{P}_w}{d\tilde{z}} \rangle$	k_{rn}	k_{rw}	λ	f_{EU}
		Eq. (1)	Eq. (3)	Eq.(4)			Eq. (14)		Eq.(15)	Eq.(15)	Eq.(16)	Eq.(17)
[ml/min]	[ml/min]	[m/s]	[-]	[-]	[mbar]	[mbar]	[N/m]	[N/m]	[-]	[-]	[-]	[-]
0.0050		9	**×10^{-5}**	0.25	20.501	34.232	1.025E+05	1.712E+05	0.0233	0.0760	0.417	0.0224
0.0075		×10^{-4}		0.38	24.337	33.551	1.217E+05	1.678E+05	0.0295	0.0775	0.517	0.0264
0.0100				0.50	24.878	33.527	1.244E+05	1.676E+05	0.0385	0.0776	0.674	0.0312
0.0125				0.63	30.923	34.291	1.546E+05	1.715E+05	0.0387	0.0759	0.693	0.0311
0.0150				0.75	36.769	34.296	1.838E+05	1.715E+05	0.0390	0.0758	0.700	0.0312
0.0175				0.88	38.435	35.197	1.922E+05	1.760E+05	0.0436	0.0739	0.801	0.0329
0.0200				1.00	43.743	57.008	2.187E+05	2.850E+05	0.0438	0.0456	1.303	0.0258
0.0300				1.50	59.283	58.514	2.964E+05	2.926E+05	0.0484	0.0445	1.481	0.0265
0.0500				2.50	82.338	74.893	4.117E+05	3.745E+05	0.0581	0.0347	2.274	0.0241
0.0750				3.75	107.558	90.981	5.378E+05	4.549E+05	0.0667	0.0286	3.172	0.0217
0.1000				5.00	125.317	101.947	6.266E+05	5.097E+05	0.0764	0.0255	4.068	0.0205
0.1500				7.50	156.651	133.695	7.833E+05	6.685E+05	0.0916	0.0195	6.401	0.0168
0.2000				10.00	197.028	156.018	9.851E+05	7.801E+05	0.0971	0.0167	7.919	0.0148
0.3000				15.00	256.103	198.126	1.281E+06	9.906E+05	0.1121	0.0131	11.604	0.0121
0.001	**0.025**	9.69	**2.394**	0.04	21.731	36.714	1.087E+05	1.836E+05	0.0044	0.0886	0.068	0.0056
0.005		×10^{-4}	**×10^{-5}**	0.20	30.278	54.930	1.514E+05	2.746E+05	0.0158	0.0592	0.363	0.0158
0.010				0.40	43.517	55.302	2.176E+05	2.765E+05	0.0220	0.0588	0.508	0.0198
0.020				0.80	45.137	63.254	2.257E+05	3.163E+05	0.0424	0.0514	1.121	0.0272
0.025				1.00	52.250	63.160	2.613E+05	3.158E+05	0.0458	0.0515	1.209	0.0282
0.040				1.60	71.690	68.000	3.585E+05	3.400E+05	0.0534	0.0478	1.518	0.0288
0.080				3.20	116.879	109.647	5.844E+05	5.482E+05	0.0655	0.0297	3.002	0.0222
0.120				4.80	144.029	124.038	7.201E+05	6.202E+05	0.0797	0.0262	4.134	0.0211
0.200				8.00	199.532	167.792	9.977E+05	8.390E+05	0.0959	0.0194	6.727	0.0169
0.250				10.00	225.260	184.310	1.126E+06	9.216E+05	0.1062	0.0176	8.182	0.0157
0.001	**0.04**	1.55	**3.831**	0.03	28.796	60.743	1.440E+05	3.037E+05	0.0033	0.0856	0.053	0.0043
0.004		×10^{-3}	**×10^{-5}**	0.10	21.578	58.164	1.079E+05	2.908E+05	0.0177	0.0894	0.270	0.0190
0.008				0.20	33.036	60.500	1.652E+05	3.025E+05	0.0232	0.0860	0.366	0.0231
0.012				0.30	44.289	61.759	2.214E+05	3.088E+05	0.0259	0.0842	0.418	0.0248
0.020				0.50	46.170	67.162	2.309E+05	3.358E+05	0.0415	0.0775	0.727	0.0326
0.040				1.00	63.346	74.746	3.167E+05	3.737E+05	0.0604	0.0696	1.180	0.0377
0.080				2.00	86.214	99.599	4.311E+05	4.980E+05	0.0888	0.0522	2.311	0.0365
0.120				3.00	107.158	109.802	5.358E+05	5.490E+05	0.1072	0.0474	3.074	0.0358
0.200				5.00	155.556	141.517	7.778E+05	7.076E+05	0.1230	0.0368	4.549	0.0301
0.400				10.00	259.205	204.070	1.296E+06	1.020E+06	0.1477	0.0255	7.873	0.0226
0.001	**0.04**	1.55	**3.831**	0.03	12.688	39.154	6.344E+04	1.958E+05	0.0075	0.1329	0.077	0.0095
0.005		×10^{-3}	**×10^{-5}**	0.13	15.463	43.311	7.732E+04	2.166E+05	0.0309	0.1201	0.350	0.0311
0.010				0.25	27.006	43.631	1.350E+05	2.182E+05	0.0354	0.1192	0.404	0.0343
0.020				0.50	49.333	64.159	2.467E+05	3.208E+05	0.0388	0.0811	0.650	0.0320
0.030				0.75	44.473	66.749	2.224E+05	3.337E+05	0.0646	0.0779	1.126	0.0413
0.040				1.00	57.907	64.507	2.895E+05	3.225E+05	0.0661	0.0806	1.114	0.0425
0.080				2.00	87.260	90.627	4.363E+05	4.531E+05	0.0877	0.0574	2.077	0.0387
0.120				3.00	111.805	94.284	5.590E+05	4.714E+05	0.1027	0.0552	2.530	0.0395
0.200				5.00	166.953	127.819	8.348E+05	6.391E+05	0.1146	0.0407	3.828	0.0323
0.400				10.00	276.704	192.623	1.384E+06	9.631E+05	0.1383	0.0270	6.961	0.0236
0.0100	**0.05**	1.938	**4.789**	0.20	22.986	54.796	1.149E+05	2.740E+05	0.0416	0.1187	0.477	0.0383
0.0500		×10^{-3}	**×10^{-5}**	1.00	65.706	75.437	3.285E+05	3.772E+05	0.0728	0.0862	1.148	0.0461
0.1000				2.00	106.743	101.952	5.337E+05	5.098E+05	0.0897	0.0638	1.910	0.0419
0.5000				10.00	316.671	218.030	1.583E+06	1.090E+06	0.1511	0.0298	6.885	0.0260
0.4000				8.00	287.735	221.396	1.439E+06	1.107E+06	0.1330	0.0294	6.156	0.0253
0.2500				5.00	231.364	186.705	1.157E+06	9.335E+05	0.1034	0.0348	4.035	0.0279
0.0400				0.80	108.234	115.543	5.412E+05	5.777E+05	0.0354	0.0563	0.854	0.0259
0.0100				0.20	78.804	100.364	3.940E+05	5.018E+05	0.0121	0.0648	0.255	0.0132
0.0050	**0.06**	2.33	**5.746**	0.08	33.246	59.640	1.662E+05	2.982E+05	0.0144	0.1308	0.149	0.0170
0.0075		×10^{-3}	**×10^{-5}**	0.13	39.554	62.095	1.978E+05	3.105E+05	0.0181	0.1257	0.196	0.0206
0.0100				0.17	44.334	62.715	2.217E+05	3.136E+05	0.0216	0.1244	0.236	0.0237
0.020				0.33	46.817	68.094	2.341E+05	3.405E+05	0.0409	0.1146	0.485	0.0374

1	2	3	4	5	6	7	8	9	10	11	12	13
$\tilde{q}_n$	$\tilde{q}_w$	$\tilde{U}_w$	$\boldsymbol{Ca}$	$\boldsymbol{r}$	$\langle\tilde{P}_n\rangle$	$\langle\tilde{P}_w\rangle$	$\langle\frac{d\tilde{P}_n}{d\tilde{z}}\rangle$	$\langle\frac{d\tilde{P}_w}{d\tilde{z}}\rangle$	k_{rn}	k_{rw}	λ	f_{EU}
		Eq. (1)	Eq. (3)	Eq.(4)			Eq. (14)		Eq.(15)	Eq.(15)	Eq.(16)	Eq.(17)
[ml/min]	[ml/min]	[m/s]	[-]	[-]	[mbar]	[mbar]	[N/m]	[N/m]	[-]	[-]	[-]	[-]
0.030				0.50	51.547	70.654	2.577E+05	3.533E+05	0.0557	0.1104	0.685	0.0449
0.040				0.67	66.649	70.992	3.332E+05	3.550E+05	0.0574	0.1099	0.710	0.0456
0.050				0.83	72.730	76.384	3.636E+05	3.819E+05	0.0658	0.1022	0.875	0.0477
0.060				1.00	75.081	80.097	3.754E+05	4.005E+05	0.0765	0.0974	1.067	0.0503
0.070				1.17	88.125	82.371	4.406E+05	4.119E+05	0.0760	0.0947	1.090	0.0494
0.080				1.33	94.229	93.441	4.711E+05	4.672E+05	0.0813	0.0835	1.322	0.0476
0.090				1.50	104.022	102.916	5.201E+05	5.146E+05	0.0828	0.0758	1.484	0.0453
0.100				1.67	114.718	104.849	5.736E+05	5.242E+05	0.0834	0.0744	1.523	0.0449
0.125				2.08	128.573	108.849	6.429E+05	5.442E+05	0.0930	0.0717	1.764	0.0458
0.200				3.33	186.720	146.855	9.336E+05	7.343E+05	0.1025	0.0531	2.622	0.0385
0.300				5.00	252.413	188.964	1.262E+06	9.448E+05	0.1137	0.0413	3.743	0.0326
0.500				8.33	340.164	245.881	1.701E+06	1.229E+06	0.1407	0.0317	6.024	0.0272
0.600				10.00	379.167	265.565	1.896E+06	1.328E+06	0.1514	0.0294	7.004	0.0257
0.001	**0.08**	3.10	**7.662**	0.01	28.219	79.735	1.411E+05	3.987E+05	0.0034	0.1305	0.035	0.0045
0.005		$\times10^{-3}$	$\boldsymbol{\times10^{-5}}$	0.06	30.831	81.044	1.542E+05	4.052E+05	0.0155	0.1284	0.164	0.0181
0.010				0.13	41.321	81.259	2.066E+05	4.063E+05	0.0232	0.1280	0.246	0.0253
0.025				0.31	50.655	87.577	2.533E+05	4.379E+05	0.0472	0.1188	0.540	0.0417
0.050				0.63	71.013	99.191	3.551E+05	4.960E+05	0.0674	0.1049	0.873	0.0489
0.080				1.00	91.684	113.404	4.584E+05	5.670E+05	0.0835	0.0918	1.237	0.0507
0.100				1.25	113.234	128.601	5.662E+05	6.430E+05	0.0845	0.0809	1.420	0.0475
0.200				2.50	191.120	179.927	9.556E+05	8.996E+05	0.1001	0.0578	2.354	0.0406
0.400				5.00	293.241	242.918	1.466E+06	1.215E+06	0.1305	0.0428	4.142	0.0345
0.800				10.00	435.924	326.819	2.180E+06	1.634E+06	0.1756	0.0318	7.497	0.0281
0.010	**0.1**	3.88	**9.577**	0.10	45.990	105.394	2.299E+05	5.270E+05	0.0208	0.1234	0.229	0.0230
0.025		$\times10^{-3}$	$\boldsymbol{\times10^{-5}}$	0.25	62.169	106.963	3.108E+05	5.348E+05	0.0385	0.1216	0.430	0.0366
0.050				0.50	82.150	114.395	4.107E+05	5.720E+05	0.0582	0.1137	0.696	0.0467
0.075				0.75	88.776	116.020	4.439E+05	5.801E+05	0.0809	0.1121	0.980	0.0555
0.100				1.00	108.151	119.126	5.408E+05	5.956E+05	0.0885	0.1092	1.101	0.0572
0.150				1.50	143.620	144.499	7.181E+05	7.225E+05	0.1000	0.0900	1.509	0.0541
0.300				3.00	243.904	209.383	1.220E+06	1.047E+06	0.1177	0.0621	2.575	0.0447
0.500				5.00	327.528	248.211	1.638E+06	1.241E+06	0.1461	0.0524	3.789	0.0415
1.000				10.00	511.587	365.910	2.558E+06	1.830E+06	0.1871	0.0355	7.152	0.0312
0.010	**0.12**	4.65	**1.149**	0.08	50.943	104.308	2.547E+05	5.215E+05	0.0188	0.1496	0.171	0.0218
0.025		$\times10^{-3}$	$\boldsymbol{\times10^{-4}}$	0.21	74.715	112.848	3.736E+05	5.642E+05	0.0320	0.1383	0.315	0.0331
0.050				0.42	78.529	123.548	3.926E+05	6.177E+05	0.0609	0.1263	0.656	0.0500
0.075				0.63	98.494	129.806	4.925E+05	6.490E+05	0.0729	0.1202	0.824	0.0543
0.100				0.83	117.073	136.503	5.854E+05	6.825E+05	0.0817	0.1143	0.972	0.0563
0.120				1.00	127.211	142.734	6.361E+05	7.137E+05	0.0903	0.1093	1.122	0.0578
0.150				1.25	149.711	156.809	7.486E+05	7.840E+05	0.0959	0.0995	1.309	0.0564
0.200				1.67	180.082	173.220	9.004E+05	8.661E+05	0.1063	0.0901	1.603	0.0555
0.500				4.17	342.762	270.634	1.714E+06	1.353E+06	0.1396	0.0577	3.290	0.0442
0.750				6.25	441.911	327.768	2.210E+06	1.639E+06	0.1624	0.0476	4.636	0.0392
1.000				8.33	523.742	377.316	2.619E+06	1.887E+06	0.1827	0.0414	6.004	0.0355
1.200				10.00	578.127	403.809	2.891E+06	2.019E+06	0.1986	0.0387	6.985	0.0338